Zn-QDs Synthesis applying simultaneously the techniques of colloidal synthesis and sol gel and phenomenon at $\mathrm{Zn}^{2+} \rightarrow \mathbf{Zn}^{3+} + \mathrm{e}^{-}$ charge transfer

M. A. Vicencio Garrido*, H. Juárez Santiesteban, and V. Carranza Téllez

Centro De Investigación en Dispositivos Semiconductores, del Instituto de Ciencias de la Universidad Autonóma de Puebla, Av. 14 Sur Col Jardines De San Manuel, Ciudad Universitaria, Puebla, Pue., México.

M. Chávez Portillo

Universidad Politécnica Metropolitana de Puebla, Popocatépetl s/n, Reserva Territorial Atlixcáyotl, Tres Cerritos, 72480 Heroica Puebla de Zaragoza, Pue., Puebla, México.

N. Carlos Ramírez

INA OE-Instituto Nacional de Astrofísica, Óptica y Electrónica, Apartado Postal 21672000 Puebla, Pue. México.

L. H. Robledo-Taboada

Tecnológico Nacional de México, Instituto de Oaxaca, Departamento de Ingeniería Industrial.

Received 9 July 2023; accepted 27 August 2024

ZnO-QD thin solid films are drop deposited on glass substrates and calcined in air atmosphere at temperatures of $60^{\circ}\mathrm{C}, 100^{\circ}\mathrm{C}, 140^{\circ}\mathrm{C}, 160^{\circ}\mathrm{C}$ and $210^{\circ}\mathrm{C}$, respectively. The samples are examined applying the techniques: Scanning Electron Microscopy (SEM), x-Ray Diffraction (XRD), Fourier transforms in the Infrared (FTIR), Photoluminescence (PL), Transmittance (%T), and absorbance α. Tauc model, the band gap $\mathrm{E_g}$ energy is evaluated. The electrical measurements of Current-Voltage (I-V), the concentration of charge carriers, mobility and resistance, are registered by Hall Effect. The morphology of the layers shows a structural configuration with stacked compact plates and flakes-like crystalline conglomerates with a fibrous appearance. The films show a Wurtzite-type crystalline phase according to the XRD diffractograms. The grain size increased by 3.6-26.1 nm . The dislocation density δ presents a gradual increase with the calcination temperature δ (lines $/\mathrm{m}^2$) 1.57-2.22. On FT-IR spectroscopy analysis, various vibrational bands are associated with the ion and by-products generated by the hydrolysis of zinc acetate dihydrate discussed. The $\mathrm{E_g}$ undergoes oscillatory and disorderly shifting towards higher photon energy, caused by faults at the crystalline lattice of $\mathrm{E_g} \sim 3.7 - 3.87\mathrm{eV}$. In optical analysis, the discontinuity located at UV-Vis region is associated in principle at $\mathrm{Zn}^{2+} \rightarrow \mathrm{Zn}^{3+} + \mathrm{e}^{-}$ charge transfer. PL spectra at UV -Vis region record the emission bands with different relative intensities. The asymmetric Gaussian curve is related to intrinsic defects in the crystal lattice. The deconvolution of the Gaussian curve generates different emission bands assigned to red (RE) at $\sim$ 770 nm, blue (BE), green (GE) at $\sim$ 492 520 nm and yellow (YE) at $\sim 570 - 600\,\mathrm{nm}$. The systematic construction of the Schottky diode is done by placing the corresponding thin film on ITO, then PEDOT: PSS was placed, then the silver contact and finally the p - n junction was identified.

Keywords: Thermal annealing temperature; absorbance; cation; intra-transitions; photoluminescence.

DOI: https://doi.org/10.31349/RevMexFis.71.011002

1. Introduction

The electronic configuration of Zn^{2+} cation is: $1s^2 2s^2 2p^6 3s^2 3p^6 3d^{10}$ and O^{2-} anion: $1s^2 2s^2 2\mathrm{p}^4$. Therefore, the Zn^{2+} cation has available $3\,\mathrm{d}^{10}$ orbitals and the oxygen anion provides the $2\mathrm{p}^4$ free electron pair available for chemical bonding by pd hybridization [1]. In the science of inorganic materials, a proposal related to optimization has emerged, through the application of an inorganic quantum dot (QDs) ZnO-QDs that provides greater energy efficiency [2]. The shape of the grain size (GS) of organic crystals can be controlled to produce a quantum confinement effect, by defining (QDs) in general terms [3]. The structural arrangement consists of placing the nanocrystals on the surface of the substrate with suitable characteristics, to obtain greater surface adhesion with the aim of improving its morphological, optical, and electrical properties. Application has been performed on a variety of nanocrystals such as zinc oxide ZnO [4]. ZnO thin solid films, an n-type semiconductor, it has a long excitonic bond $\sim$ 60 meV, band gap $\mathrm{E_g}$ energy $\mathrm{E_g} \sim 3.7$ eV, a wide luminescence region, in addition to possessing extraordinary morphological, structural, optical, and electrical properties, for potential application in the construction of photovoltaic devices, and a variety of fields such as the biosensor, rubber industry, at inhibiting certain food-borne pathogens, pharmaceutical industry, cosmetics, optoelectronics and agriculture [5,6,7]. In order to prepare inorganic ZnO nanocrystals, various experimental synthesis techniques associated with optimal chemical and physical parameters of crystalline growth have been reported [8]. We cite only a few of these in this paper: Sol-gel is an economical and simple method [9]. The quantum confinement

effect has driven the development and investigation of colloidal semiconductor nanocrystals over approximately the past decades. V arious studies carried out on $\mathrm{ZnO}-\mathrm{QDs}$, obtained through the colloidal synthesis technique, have acceptable relative thermodynamic stability associated with a wide variety of optical properties [10]. However, the disadvantage with respect to poor and weak adhesion in film format makes its applications in devices difficult, for this reason, it has been proposed to apply the ZnO-QDs to improve adhesion in films [11]. A crystalline growth parameter is investigated and applied to obtain ZnO-QDs in order to examine the effect of quantum confinement, located at the emission edge recorded at UV-Vis region, which is associated with the gradual reduction of the GS of the crystal growth. In interesting spectroscopic studies, using photoluminescence (PL) spectra, various emission bands are examined in inorganic materials with strong relative intensity situated at UV-Vis-region associated with intrinsic crystalline defects. It is indicated that the Vis emission of $\mathrm{ZnO}-\mathrm{QDs}$ can be ascribed to singly ionized oxygen vacancies and interstices, which is related to the color centers with electron paramagnetic resonance [12], as well as, on the deformation of the crystal structure and the dynamics of structural native defects. On the other hand, the phenomenon of quantum confinement and its correlation with the dimension of GS with gauge dimensions has been extensively investigated in depth and exhaustively. The relatively low growth temperatures reduce the diffusion of ions, atoms, or molecules at the surface, which leads to morphological and chemical changes. Indeed, the concentration of the progenitor reagents can alter the morphology of $\mathrm{ZnO}-\mathrm{QDs}$ nanocrystals [13]. In this manuscript, the chemical synthesis and some intrinsic properties of $\mathrm{ZnO}-\mathrm{QD}$ are examined, to make thin solid films by the dripping method, with a thickness of $\sim 800\,\mathrm{nm}$, annealed in a temperature range at $\sim 60-210^{\circ}\mathrm{C}$, to monitor the crystallographic growth of nanocrystals, and investigate their morphological, structural, optical, electrical properties and their application as a Schottky-diode with the p-njunction, under a hybrid structure with PEDOT: PSS and compared to thin films of QD's ZnO.

2. Experimental

2.1. ZnO-QDs by Sol-Gel technique

The Sol-Gel method, is an experimental chemical synthesis technique that allows obtaining a wide variety of crystalline nanostructures with relative ease, choosing a low relative reaction temperature, using a sol and a gel, respectively. It is perhaps better defined more broadly as covering the synthesis of solid nanocrystals such as metal oxides from solution-state precursors [14]. The experimental method is relatively inexpensive, fast, efficient, and has acceptable experimental reproducibility for preparing various inorganic oxides, particularly $\mathrm{ZnO}-\mathrm{QDs}$. The sol-gel synthesis process used in this document is the following: the addition of ~ 14.1 mLs of methanol and ~ 0.5 mLs of MEA (monoethanol amine), maintaining constant stirring for ~ 15.0 min, then ~ 1.5 g of zinc acetate dihydrate $(\mathrm{Zn(COO)_2 \cdot 2H_2O})$, the solution thus obtained is stirred vigorously for ~ 30.0 min at room temperature.

2.2. Technique applied in the Colloidal Synthesis of ZnO-QDs

Now, study, analysis and experimentally preparing ZnO-QDs using the Colloidal-Synthesis technique, is carried out while maintaining the previously reported experimental conditions [15]. Potassium hydroxide $(\mathrm{KOH})0.8\mathrm{M}$ dissolved in methanol is mixed at a temperature of $\sim 60^{\circ}\mathrm{C}$ for ~ 30 min, then $\mathrm{Zn(COO)_2 \cdot 2H_2O}$ dissolved in methanol is added to obtain the solution containing the ZnO nanoparticles. The experimental chemical synthesis is carried out with the systematic control of temperature, a parameter that allows implicit monitoring of the size and intrinsic crystalline structural properties. Once the material to be investigated has been obtained through the optimal experimental stages and conditions, the product is purified to eliminate by-products generated in the chemical reaction. The solvent used here is eliminated using a rotary steamer at a temperature of $\sim 50^{\circ}\mathrm{C}$, to obtain 20 mLs of this solution. The purification process at a 1:5:1 ratio of $\mathrm{ZnO}-\mathrm{QDs}$ in methanol + hexane + isopropanol. The experimental process was repeated three consecutive times to avoid contamination with by-products. 2.3. $\mathrm{ZnO}-\mathrm{QDs}$ thin solid films prepared by calcination at temperatures of $60^{\circ}\mathrm{C}$, $100^{\circ}\mathrm{C}$, $140^{\circ}\mathrm{C}$, $180^{\circ}\mathrm{C}$ and $210^{\circ}\mathrm{C}$, respectively.

The slide glass substrates are previously washed with chromic solution to ensure the surface is free of grease and adhered pollutants [16]. The ZnO-QDs were chemically synthesized, mixing the two previously prepared solutions following the steps proposed in sections 2.2 and 2.2, respectively. The optimal proportion in relation to volumes was recorded in a 1:1 ratio, to obtain the optimal amount of both compounds. The layers deposited on the substrate are then prepared using the standard drop method. The samples are treated individually at the calcination temperature in an air atmosphere for $\sim 30,0\,\mathrm{min}$ at $60^{\circ}\mathrm{C}$, $100^{\circ}\mathrm{C}$, $140^{\circ}\mathrm{C}$, $180^{\circ}\mathrm{C}$ and $210^{\circ}\mathrm{C}$, respectively. Thin films are labeled using the following symbols: MZN-1, MZN-2, MZN-3, MZN-4 and

TABLE I. Codes assigned to the thin films treated at the corresponding calcination temperature.

Sample	calcination temperature $(^{\circ}\mathrm{C})$
MZN-1	60
MZN-2	100
MZN-3	140
MZN-4	180
MZN-5	210

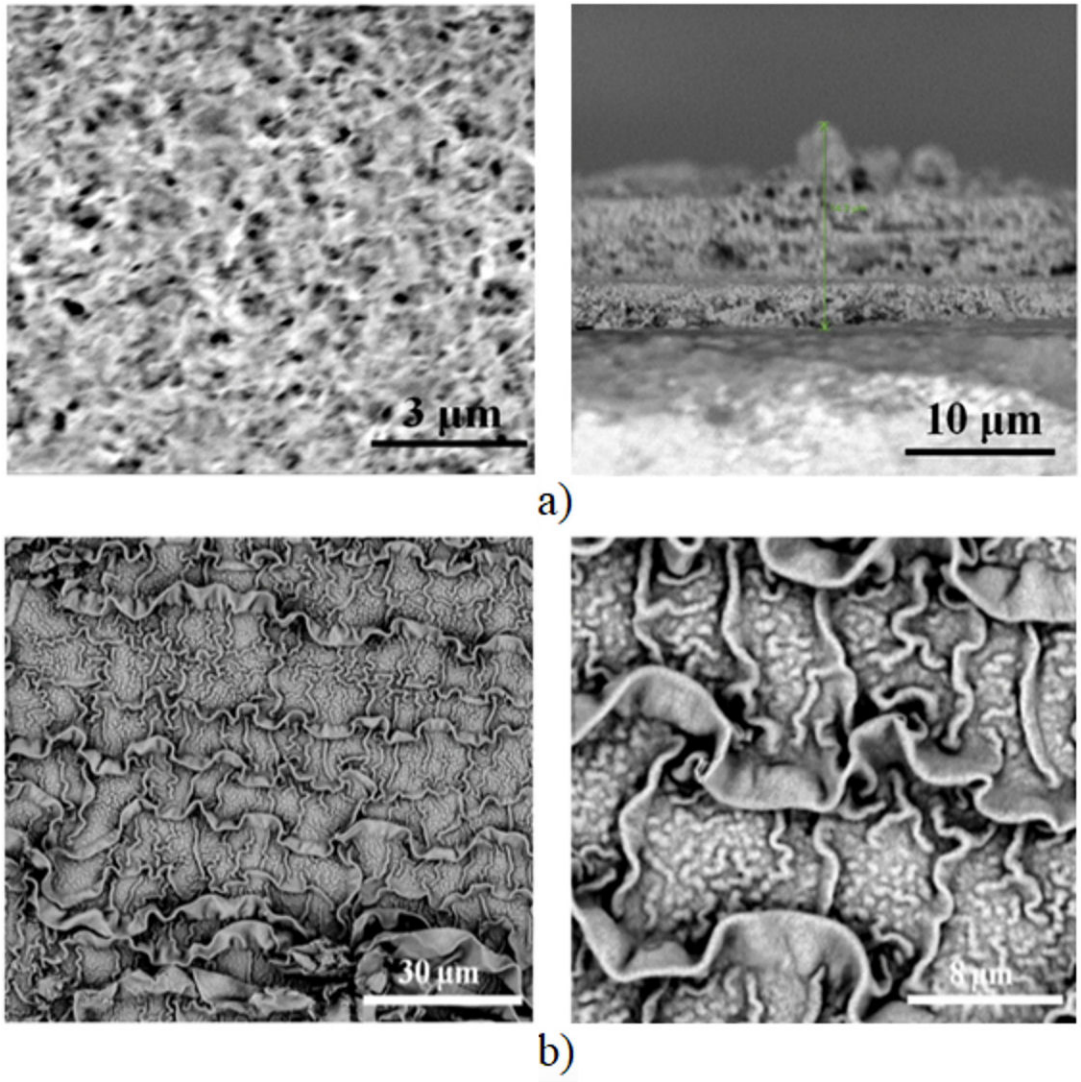

FIGURE 1. Scanning Electron Microscopy (SEM) micrographs of a) MZN-1 b) MZN-5 thin solid films.

MZN-5 according to the calcination temperature, respectively. Table I shows the symbolic keys assigned to the films treated at the corresponding calcination temperature.

The X-ray Diffraction (XRD) patterns were characterized by the Bruker Discover model D8 equipment, $\mathrm{Cu}-\mathrm{K}_{\alpha}$ radiation $\lambda \sim 0.154\,\mathrm{nm}$ at range $20^{\circ} \leq 2\theta \leq 80^{\circ}$, which operates at 40 mA and 40 k. UV-Vis spectra were recorded using a Thermo Scientific spectrophotometer (evolution 600 model) in absorbance mode. Photoluminescence spectra are recorded using a 325 nm, 60 mW He-Cd laser, Sciencetech Model 6040 half-meter monochromator, Sciencetech LIA 100 blocking amplifier, and a silicon PIN photodetector.

3. Results and discussion

3.1. Scanning electron microscopy

Scanning electron microscopy (SEM) images were made with the sem phenom pro X equipment. Figure 1 shows SEM images of a) MZN-1 and b) MZN-5 thin films. In the cross section in the thin solid film shown in Fig. 1a), fibers of different lengths and crystal flakes-like fibers create layers of crystalline conglomerates overlapping each other and regions with non-uniformly distributed voids are appreciated. However, in the samples in Fig. 1b), a compact and uniform surface can be seen presenting crystalline flakes-like limited by very thin crystalline lines. The surface morphology of materials undergoes modification by the effect of thermal treatment and is governed by the desorption of some contaminants adhered to the surface and the volume of the sample. Generally, a drastic dependence on the experimental conditions related to the crystalline growth parameters used is associated. It is evident that the calcination temperature is a key and necessary parameter to understand in greater depth the conditions to find the optimal experimental conditions for the morphological properties when applying the present technique of chemical synthesis. The calcination temperature increases the surface energy in the layers and also tends to become

higher, which causes smaller particles, to fuse with the neighboring particles thus, forming a larger crystallite size [17].

3.2. X-Ray diffraction

The X-Ray diffraction (XRD) characterization technique was applied in this report to examine the structural properties of the compounds. Figure 3 shows the XRD diffractograms of MZN-1, MZN-2, MZN-3, MZN-4 and MZN-5 layers. We perform the angular sweep 2 2θ located at range $2\theta \sim 20° - 70°$. The crystallographic planes of reflection examined are assigned at (002) and (103) crystalline planes, which correspond to the Wurtzite crystalline phase, according to the standards (JCPDS36-1451). The recorded planes present a full width at half maximum (FWHM) difference, a structural phenomenon commonly associated with the creation of nanocrystals with small grain size (GS) dimensions, as well as amorphous regions [18]. The crystal plane oriented in the preferential direction (002) is associated with the surface energy density of greater minimum relative crystal energy stability. Each Zn2+ cation layer is driven to grow along the exposed closest packed plane (002), leading to compact and planar ZnO-QDs deposition [19]. Therefore, the FWHM shown in the crystallographic planes is associated with an increase in the calcination temperature. The microstructural behavior can be tentatively justified and associated with the stages involved in the nucleation phenomenon and crystalline growth. Although the nucleation phenomenon is complex, interest should not be lost in finding the correlation between chemical and physical parameters that formally govern the morphological phenomenon. The crystals precipitate on the pores' surface, modify the pore space morphology, and reduce their flow and transport properties [20]. However, the phenomenon of nucleation followed by growth and, in turn, the creation of fine nanoparticles with different GS averages, governed by the calcination temperature [21]. The microstructural behavior is directly related to the average grain size (GS) calculated using the Scherer's equation [22]

$$D = \frac{k\lambda}{\beta \cos\theta},$$

where λ is the wavelength of X-ray radiation ~ 0.154 Å, k the Scherer's constant $(k \sim 0.9), \theta$ (in radians) the characteristic X-ray radiation, and β is FWHM of the crystalline plane (in radians). The average GS was calculated using the recorded experimental data of the FWHM obtained from the XRD experimental results, finding a grain size from 3.6 nm to 6.9, which indicates a quantum effect in the $\mathrm{ZnO} - \mathrm{QD}$'s mixture. For the sample $\mathrm{Mx} - 1$ we have a quantum size of 3.6 nm with heat treatment of $60°\mathrm{C}$, but in the following $\mathrm{MX} - 2, \mathrm{MX} - 3, \mathrm{MX}$ 4, and MX5 samples the temperature of the heat treatment is gradually increased until the temperature of $210°\mathrm{C}$ is reached in one of the films, to promote the necessary energy of nanoparticle growth in thin films, reaching a nanoparticle size of up to 6.9 nm , where at this size the ZnO comes to present weak quantum confinement, according

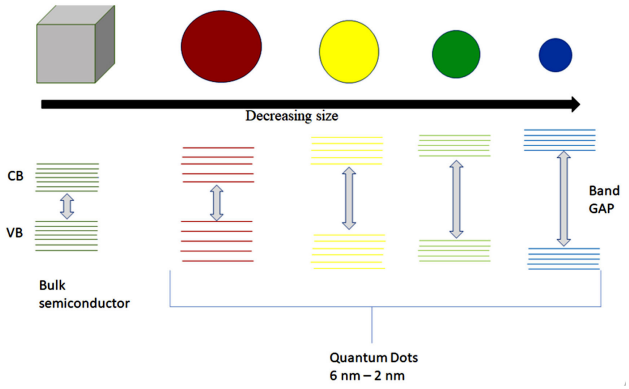

FIGURE 2. Discretization of Quantum Dots bands.

to the size of the Bohr succession diameter for the ZnO which is 2.4 nm , the process of quantum confinement is directly related to the variation of the semiconductor GAP, photoluminescence and with the discretization of the energy bands, as shown in Fig. 2. By varying the temperature in the thin films, it also promotes the reduction of structural defects, intrinsic to the ZnO material as oxygen vacancy, of zinc and interstices that will be of great help to realize the P-n junction, as will be studied later [23].

Table II shows grain size (GS), calcination temperature, FWHM β, microstrain ε, dislocation density δ of MZN-1, MZN-2, MZN-3, MZN-4 and MZN-5 layers. Calcination temperature is a key parameter that obeys the microstructural properties of layers. The microstructural behavior can be considered by the sliding effect of $\left(\mathrm{Zn}^{2+}\right)$ cations, $\left(\mathrm{O}^{2-}\right)$ ions, atoms and molecules, and other non-specific rearrangements, generating the crystal lattice's deformation. These design principles are based on the assumption of compositional and structural rigidity, as measured crystallographically. It is necessary to mention that it is a phenomenon that is difficult

TABLE II. Grain size (GS), calcination temperature, FWHM β, microstrain ε, dislocation density δ of MZN-1, MZN-2, MZN-3, MZN-4 and MZN-5 layers.

sample	(hkl)	2θ	β	Grain Size (nm)	Microstain $\varepsilon \times 10^{-3}$	Dislocation density δ(lines/m^2)
MZN-1	(100)	33.04	0.32	25.1	0.42	1.57×10^{15}
	(002)	34.89	0.84	3.6	3.65	7.49×10^{16}
MZN-2	(100)	33.01	0.42	19.7	0.54	2.56×10^{15}
	(002)	33.95	2.10	3.9	2.8	6.41×10^{15}
MZN-3	(100)	33.01	0.37	21.8	0.49	2.09×10^{15}
	(002)	33.92	1.29	6.4	1.72	2.43×10^{15}
MZN-4	(100)	33.02	0.38	21.5	0.47	2.13×10^{15}
	(002)	33.95	1.73	4.7	2.31	4.37×10^{15}
MZN-5	(100)	33.08	0.39	21.1	0.50	2.22×10^{15}
	(002)	33.83	1.89	6.9	1.57	2.05×10^{15}

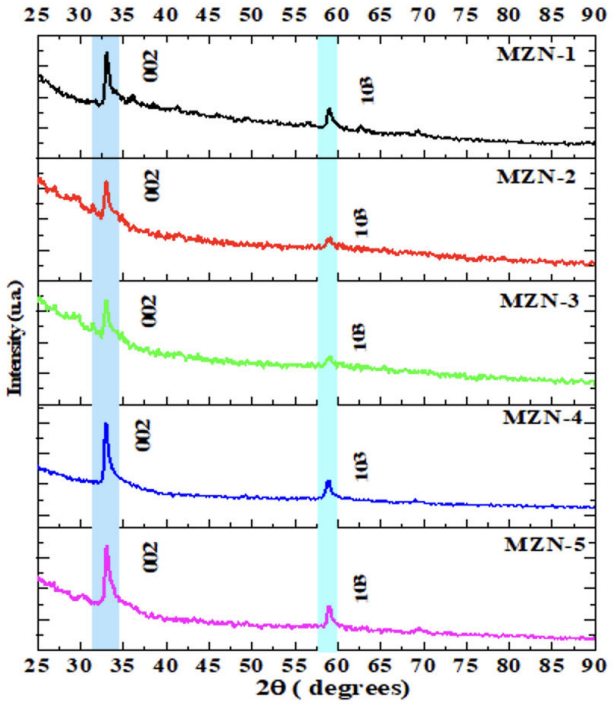

FIGURE 3. XRD diffractograms of MZN-1, MZN-2, MZN-3, MZN-4 and MZN-5 samples.

to predict with certainty. It is interesting to investigate through a theoretical-experimental analysis and to propose it at each stage carried out in the calcination treatment. The crystals' growth and the transition from nano- to micro-size occurred at $\sim 700°\mathrm{C}$ [24].

3.3. Spectroscopic analysis of the Fourier transforms in the infrared (FTIR)

Figure 4 shows FTIR spectra of MZN-1, MZN-2, MZN-3, MZN-4 and MZN-5 layers. It is inferred that the samples have absorption bands located at $\sim 462\ \mathrm{cm}^{-1}$, $\sim 670\ \mathrm{cm}^{-1}$, $\sim 1090\ \mathrm{cm}^{-}\ 1$, $\sim 1158\ \mathrm{cm}^{-1}$, $\sim 1325\ \mathrm{cm}^{-1}$, $\sim 1390\ \mathrm{cm}^{-1}$, $\sim\ 1545\ \mathrm{cm}^{-1}$ and $\sim\ 3256\ \mathrm{cm}^{-1}$. Vibration modes located at $\sim 400-1600\ \mathrm{cm}^{-1}$ assigned to the CO_3^{2-} anion [25].

We have reported absorption bands at $\sim 400-3600\ \mathrm{cm}^{-1}$ range as associated to vibrations in CO_3^{2-} anions and the progenitor reagent that generates this ion in aqueous solution [26]. The absorption mode situated at $\sim 1390\ \mathrm{cm}^{-1}$ is connected with the asymmetric stretching vibrations of CO_3^{2-} is assigned to the bending out plane vibration modes. In all FTIR spectra, an intense band is located at $\sim\ 1323\ \mathrm{cm}^{-1}$, which was attributed to asymmetric stretching vibrations of the CO_3^{2-} groups. Such absorption band, due to CH_3COO^{-} fragmenting (was induced by our working conditions) pH, stirring time growth. For MZN-1, MZN-2, MZN-3 and MZN-4 thin solid films, a broad absorption band in the $\sim\ 3256\ \mathrm{cm}^{-1}$ region can be attributed to stretching of the - OH groups of defective sites and the physically adsorbed

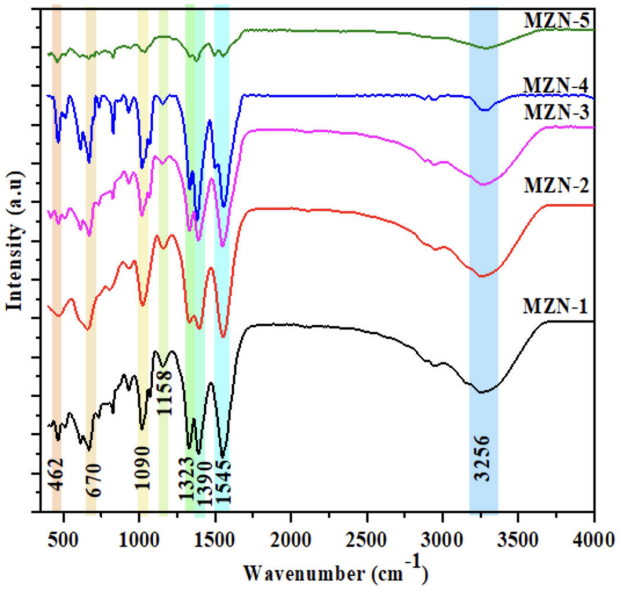

FIGURE 4. FTIR spectra of MZN-1, MZN-2, MZN-3, MZN-4 and MZN-5 thin solid films.

water H_2O molecules (or hydrated) adsorbed on the hydroxide surface. The band located at $\sim\ 1123\ \mathrm{cm}^{-1}$ shifted to high wavenumbers due to a large number of point defects at the surface of nanoparticles, which are characteristic defects reported for these nanocrystals [27]. The absorption mode at $\sim\ 472\ \mathrm{cm}^{-1}$ corresponds to metal-oxygen (ZnO stretching vibrations) vibration mode. The absorption band at $\sim\ 1005\ \mathrm{cm}^{-1}$ is ascribed to the stretching vibration of $-\mathrm{C}-\mathrm{N}$ bond of the primary amine or to the stretching vibration of the -C-O bond of the primary alcohol. Generally, these by-products are associated with the hydrolysis of zinc acetate dihydrate (Zn(CH3COO)2), and the alkaline medium of chemical synthesis. The absorption bands situated at $\sim\ 1090\ \mathrm{cm}^{-1}$, $\sim\ 1325\ \mathrm{cm}^{-1}$, and $\sim\ 1390\ \mathrm{cm}^{-1}$ ascribed to primary, secondary alcohol in-plane bend or vibration. The absorption band at $\sim 1595\ \mathrm{cm}^{-1}$ is ascribed to the vibration modes of aromatic nitro compounds and alkyl ascribed to the stretching vibration of hydroxyl compounds. The sample is labeled according to the MZN-5 symbology; the absorption band assigned to the H_2O molecules almost completely disappears due to the calcination temperature. In addition, a decrease in the relative intensity of the bands identified with the carbonate ion and contaminants incorporated in the crystalline growth can be seen.

3.4. UV-Vis spectroscopy

The spectral analysis of transmittance $\%$ T, and absorbance α of all samples, is performed in the UV-Vis region situated at a range $\sim\ 300\ -\ 700$ nm ($\sim\ 4.13\ -\ 1.77$ eV). Figure 5 shows the $\%$ T vs. wavelength λ spectrum of MZN-1, MZN-2, MZN-3, MZN-4 and MZN5 thin solid films. The optical behavior in % T presents a gradual relative increase of ~ 20 85 % due to the increase in the calcination temperature. In

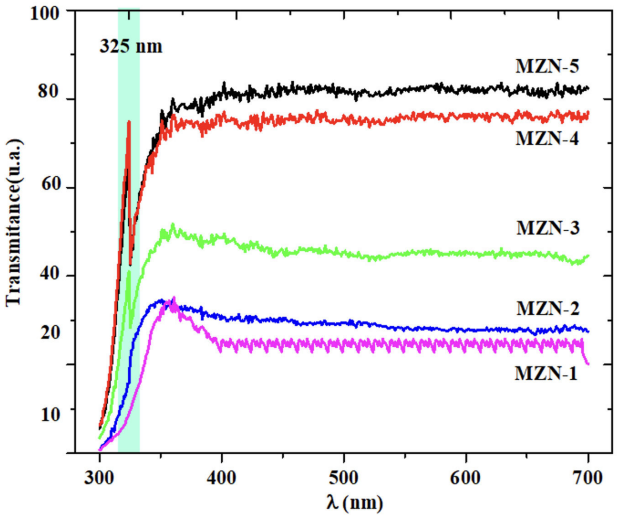

FIGURE 5. Transmittance (% T) vs. wavelength λ spectrum of MZN-1, MZN-2, MZN-3, MZN-4 and MZN-5 thin solid films.

particular, MZN-3, MZN-4 and MZN-5 samples, present a drastic jump at % T concerning MZN-1, MZN-2 thin films, with a $\%$ T minimum. The abrupt jump in the % T located at $\sim$ 325 nm $\sim$ 3.81eV is tentatively associated with the charge-transfer from the Zn^{2+} to Zn^{3+} cation, processes between electron-rich and electron-poor counterparts, typically resulting in a new absorption band at a higher $\boldsymbol{\lambda}$. Diffraction (002) is larger in the MX-1 sample (Fig. 2), concerning the others, since it is directly related to the quantum size of the nanoparticle, obtained by Scherrer's equation of approximately 3.6 nm , which tells us that we have the presence of ZnO quantum dots, this quantum size is related in the UV-Vis by the shift in the absorbance indicating the presence of quantum confinement, not so in the energy transition since the generated ZnO has a large number of defects present that promote the phenomenon of the recombination of electrons, that by increasing the temperature they are eliminated thus allowing to observe the phenomenon of the energy transition. During thermal annealing, disordered atoms in the material can gain mobility, allowing them to rearrange into a more ordered crystalline structure. As the crystallinity improves, the XRD peaks become sharper and more intense [28]. This discontinuity in the optical curve of the $\%$ T is difficult to obtain; the behavior is interesting and requires careful study, which we will return to later.

Figure 6 shows the absorbance α vs. wavelength λ spectrum of MZN-1, MZN-2, MZN-3, MZN-4 and MZN-5. The absorption bands (AB) located at $\sim$ 365 nm ($\sim$ 3.97 eV) observed with higher magnification in films MZN-4 and MZN-5 samples, are assigned to the fundamental electronic transition CB $\rightarrow$ VB of ZnO [29]. The absorption bands (AB) located at $\sim$ 365 nm($\sim$ 3.97eV) observed with higher magnification at MZN-4 and MZN-5 are assigned to the fundamental CB $\rightarrow$ VB electronic transition of ZnO [10]. In MZN-4 and MZN-5 samples, showing a significant shift towards greater λ at AB, detectable within the error threshold. The reaches

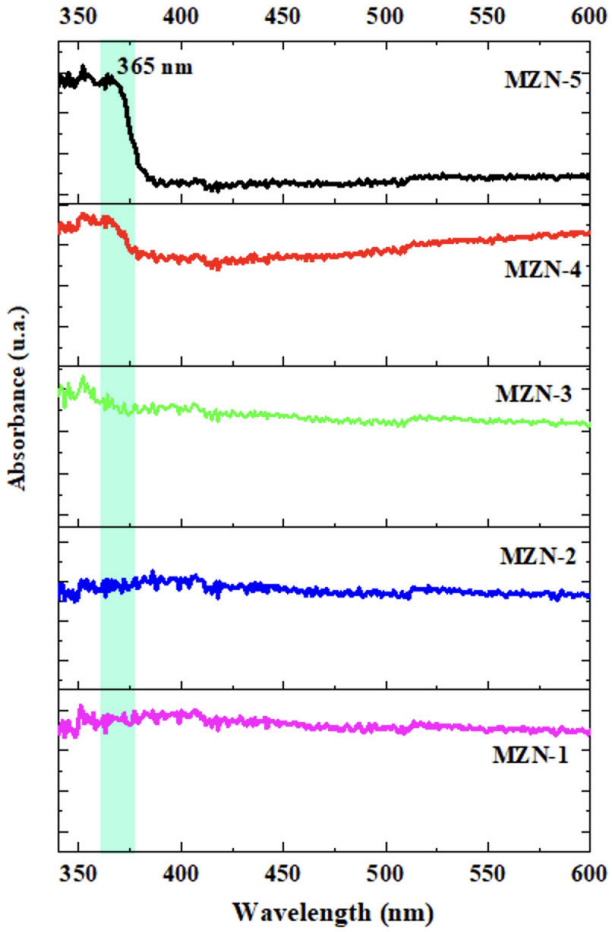

FIGURE 6. Absorbance vs. wavelength spectrum of MZN-1, MZN-2, MZN-3, MZN-4 and MZN-5 layers.

a relative maximum of $\sim$ 80$\%$ localized at $\sim$ 350 nm ($\sim$ 3.54 eV), then remains unchanged for $\lambda > 350$ nm. It is observed in the samples MZN-1, MZN-2, MZN-3, α registered is relatively low; this is associated with intrinsic defects. It is observed at MZN-1, MZN-2, MZN-3 layers, α registered is relatively low, and is associated with intrinsic defects [30]. The optical phenomenon is associated with intrinsic crystallization failures in the chemical synthesis process presented here. The variations in the relative intensity of the ABs are correlated with the superficial and volumetric morphology associated with energy levels created by intrinsic crystalline defects, free charge transfer from the passage of Zn^{2+} $\left(3\,d^{10}\right)$ to Zn^{3+} $\left(3\,d^{9}\right)$ cation, stacking failures, microstrain, noncrystalline compaction, homogeneous, faults in grain boundaries etc. The phenomenon is associated with the gradual increase of the GS, calcination temperature, FWHM β, microstrain ε, and dislocation density δ with modification of intrinsic crystalline defects, critically modifying the optical properties. The optical phenomenon can in principle be associated with the crystalline disorder and chaotic fault creation, resulting in the creation of discrete energy levels and deep traps associated with free charge carriers, thus polarizing the electronic cloud. An AB situated at the visible range

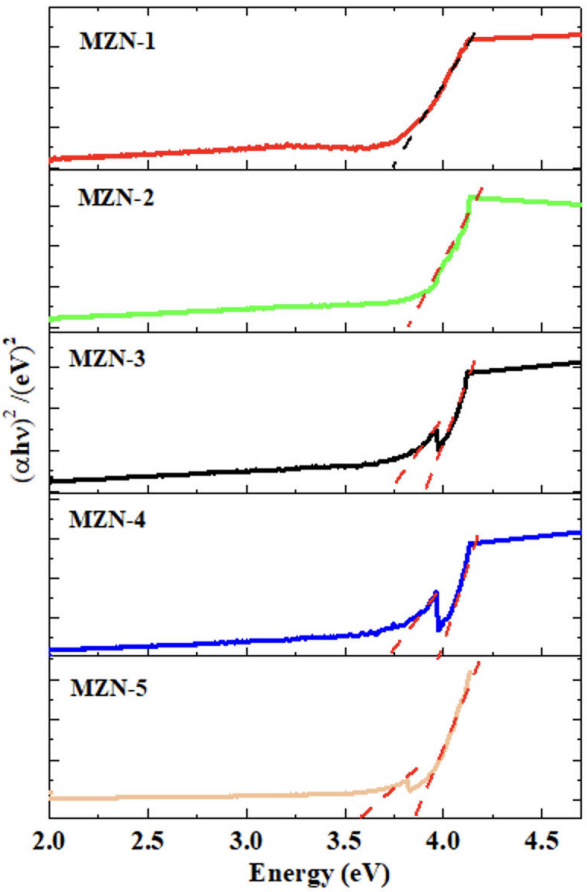

FIGURE 7. $(\alpha hv)^2$ vs. E(eV) spectrum of MZN-1, MZN-2, MZN-3, MZN-4 and MZN-5 thin solid films.

that is not apparent in the separated materials emerges when the interface is formed. Interestingly, photoexcitation of this interface band or band-to-band results in a counterintuitive photovoltaic response when a supra/sub-band-gap light is shone [31]. The optical phenomenon can be associated with the crystalline disorder and chaotic fault formation, resulting in the creation of discrete energy levels and deep traps associated with free charge carriers, thus polarizing the electronic cloud. However, in MZN-4, MZN-5 thin films, a significant difference is manifested in the region located at $\sim 350-375$ nm ($\sim 3.54-3.30$ eV) is registered. A sudden jump of α located in the UV-region, specifically situated at ~ 365 nm (~ 3.39 eV), is observed at MZN-4, MZN-5 layers. On the other hand, we have that the ionic chemical bond for ZnO is the result of the mixture of dsp orbitals and it is possible to tentatively associate it with the charge transfer phenomenon: $Zn^{2+} \rightarrow Zn^{3+} + e^{-}$n (defect-emission free) in this material [32].

The band gap E_g energy of the material is related to the optical absorption, according to the interesting Tauc eq. $\alpha hv = A\,(hv - E_g)^x$ where A is a constant, α absorbance coefficient, hv energy of the incident photon, and x for electronic direct band transition assigned the value of $1/2$. The

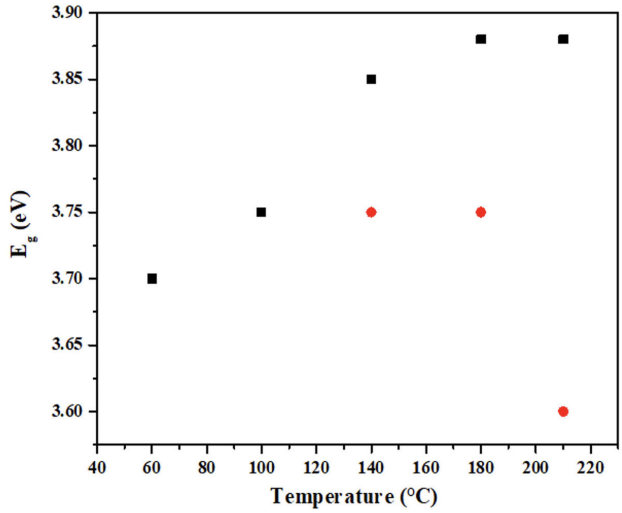

FIGURE 8. Band gap E_g energy of MZN-1, MZN-2, MZN-3, MZN-4 and MZN-5 layers.

graphical method to numerically quantify E_g consists of drawing a straight line that intersects the axis of energy $(\alpha = 0)$. Figure 7 displays ahv^2 vs. $E(\mathrm{eV})$ spectrum of MZN-1, MZN-2, MZN-3, MZN-4 and MZN-5 thin films and Fig. 8 shows the spectrum of $E_g(\mathrm{eV})$ vs, calcination temperature $(^{\circ}\mathrm{C})$ of all the thin solid films. Reports of the optical behavior of the fundamental electronic transition $\mathrm{CB} \rightarrow \mathrm{CV}$ of ZnO , which is often attributed to direct recombination in the inverted electron-hole plasma [33], identified and assigned to the phenomenon of recombination of energetic excitons that are tightly bound and dominate the optical response even at room temperature [34]. The MZN-1, MZN-2 samples, present the slope associated with the $\mathrm{E_g}$ defined according to the aforementioned graphic method. In the case of MZN-3, MZN-4 and MZN-5 layers, two electronic transitions are very close to each other.

As a first approximation, the optical behavior is associated with charge transfer, considering the $\mathrm{Zn(pd)}$ and $\mathrm{O(sp)}$ orbitals very close to each other. The intra-electronic transition phenomenon reduced to a $Zn^{2+} \rightarrow Zn^{3+} + e^{-}$(defect-emission free) [32]. Tentatively, we propose charge transfer of the Zn^{2+} and Zn^{3+} cation, is an optical phenomenon observed here. However, this optical behavior requires a detailed study to be describe in more depth [35].

3.5. Photoluminescence

The experimental Photoluminescence (PL) spectroscopic technique is applied to investigate the emission bands (EB) associated with intrinsic crystalline defects (vacancies, interstices, and the introduction of color centers) and the optical behavior of E_g in inorganic single crystals. The EB registered in the UV-Vis region by PL is considered an optical phenomenon originated by radiative recombination of acceptors and charge donors, which significantly affects charge photogeneration [36]. Figure 9 shows the PL spectrum of a) MZN-1, b) MZN-2, c) MZN-3, d) MZN-4 and e) MZN-5 samples.

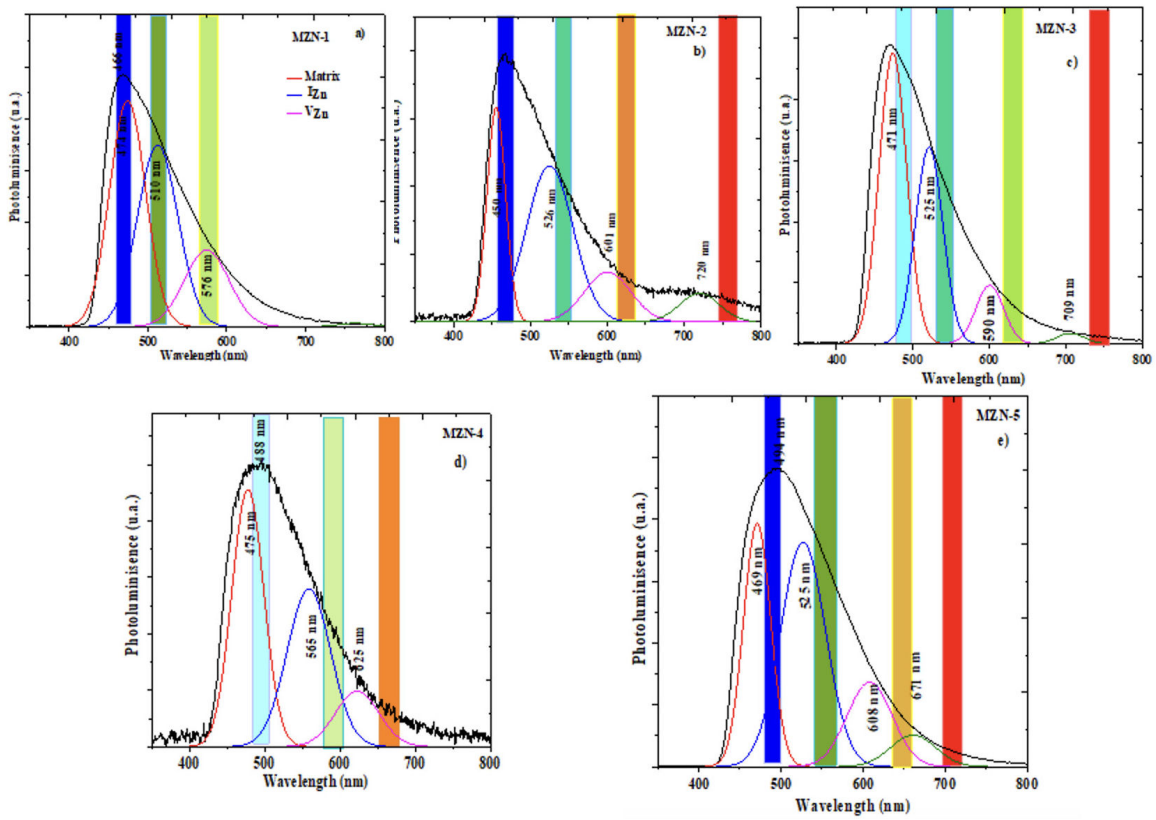

FIGURE 9. Deconvoluted Photoluminescent vs. Wavelength spectra of a) MZN-1, b) MZN-2, c) MZN-3, d) MZN-4 and e) MZN-5 thin solid films.

The Gaussian curve of thin films, presents a non-symmetric geometry dependency (or asymmetry) at EB. The asymmetric optical behavior is interpreted geometrically as the superposition of two or more signal bands, for this reason, we proceed to carry out the deconvolution and investigate its origin. We use a differently colored fringe on the symmetrical Gaussian curve in order to facilitate quick identification of the corresponding emission band. The deconvolution of the asymmetric Gaussian curve generates three symmetric EB of different relative intensities located in the region $\sim 400-700$ nm $\sim 3.10-1.77$ eV. Crystal defects of ZnO have been identified and extensively investigated, assigning their origin with crystallographic characteristics commonly to zinc $(\mathrm{V_{Zn}})$ and oxygen $(\mathrm{V_O})$ vacancies among other crystal faults [37-40]. Table IV compiles the electronic transitions and intro transitions of MZN-1, MZN-2, MZN-3, MZN-4 and MZN-5 thin films. In all the samples, EB located in the UV-Vis region is observed, these show the overlap between them, which is typical in asymmetric emission signals, which are strongly governed by the blue (BE) and yellow emission bands (GE). These defects, of course, produce all the residual emissions in addition to the desired laser line [41]. The deconvolution of the Gaussian curve allows for observing symmetric emission signals. The deconvolution of the Gaussian curve shows an oscillatory and gradual increase in optical intensity [41,42]. It is possible to determine approximately the correlation that exists between the optical behavior and the intrinsic crystalline defects (see Table I). All thin solid films, present a broad emission band identified as a blue emission (BE) band associated with zinc interstices $(\mathrm{Zn_i})$ located at $\sim 450-550$ nm $(\sim 2.75-2.25$ eV) and zinc vacancies $(\mathrm{V_{Zn}})$, located at $\sim 525-750$ nm $(\sim 2.63-1.65$ eV) [42]. Symmetrical emission signals assigned at the emission band:

TABLE III. Electronic transitions and intra-transitions of MZN-1, MZN-2, MZN-3, MZN-4 and MZN-5 layers.

Wavelength (nm)	E(eV)	Defect
457	2.77	Zn_i
466	2.66	Zn_i
469	2.64	Zn_i
474	2.67	Zn_i
488	2.54	V_z
510	2.24	V_z
565	2.19	V_o
525	2.36	V_o
576	2.15	V_o
608	2.03	V_o
625	1.98	V_o
671	1.84	V_o^{++}

TABLE IV. Effect Hall of MZN-1, MZN-2, MZN-3, MZN-4 and MZN-5 thin solid film.

Sample	MZN-5	MZN-4	MZN-3	MZN-2	MZN-1
N_D (cm^{-3})	1.45×10^{14}	1.33×10^{14}	1.26×10^{14}	1.11×10^{14}	—-
Mobility (cm^2/Vs)	64.1	60.2	52.7	48.9	—-
Resistivity (Ω.cm)	6.48×10^2	7.8×10^2	8.77×10^2	2.5×10^3	—-
Type	n	n	n	n	—-

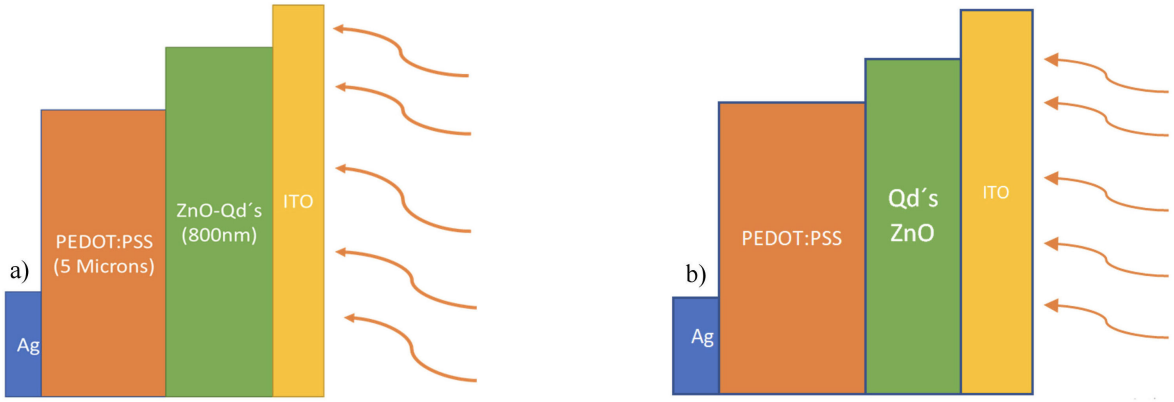

FIGURE 10. Diagram of the structural arrangement of the Schottky diode using ZnO-QDs Vs Qd's ZnO.

green (GE) situated at range $\sim 492 - 520$ nm ($\sim 2.50 - 2.38$ eV), yellow (YE) at $\sim 570 - 600$ nm ($\sim 2.17 - 2.06$ eV) and red (RE) at ~ 770 nm (~ 1.61 eV). The energy level corresponding to Zn_i lies just below the conduction band, and it can trap photo excited electron e^- followed by its radiative recombination with holes h^+ in the valence band [43]. These defects are associated with doubly ionized vacancies V_0^{++} and attributed to oxygen vacancies (V_0) and oxygen interstices (O_i). The BE is related to the transition of the V_{zn} or oxygen antisites (O_{zn}) in the conduction band (CB). The GE band assigned to the electronic transition of deep defects from V_O and from Zn_i to BV, is probably caused by the transition of localized surface charge donors. The Y E band is related to oxygen interstices (O_i), attributed to the stoichiometric imbalance created by excess oxygen, and the RE band with V_0 is located below the ZnO conduction band. The relative decrease in crystalline defects is associated with the creation of deep levels assigned to RE and located at $\sim 681 - 770$ nm ($\sim 1.82 - 1.61$ eV).

3.6. Hall effect

ND(cm-3) charge carrier concentration, resistivity and mobility are recorded using Hall effect equipment. We found that the MZN-1, MZN-2, MZN-3 and MZN-4 layers show various crystalline defects (see Table II), in a lower relative proportion compared to the MZN-5 sample. Table IV shows the compilation of the experimental results recorded at room temperature (RT) of the electrical properties of all solid thin films. The existence of native defects of the material avoids the realization of the electrical measurement in the sample MZN-1, while in the samples MZN-2, MZN-3, MZN-4, MZN-5 with increasing temperature of the heat treatment, the intrinsic defects of the material decrease, which makes possible the measurement of the electrical properties, for which there is no representative variation due to the temperature range. The types of crystalline defects in the specific application should be defined or differentiated according to whether they are desirable or undesirable.

3.7. Application of the thin solid film in the construction of the Schottky diode of ZnO Qd's and Qd's ZnO

According to the results reported in the previous work of $ZnO - Qd$'s [15], it can be considered an improvement in the electrical properties when using the $ZnO - Qd$ ds material, such as ND, mobility, and decrease in resistance. To compare the behavior and effect of ZnO-Qd's material Vs ZnO Qd's are applied as a Schottky diode, using PEDOT:PSS as "p" type material.

The silver contacts used are to ensure the Ohmic contact; silver has a higher work function than PEDOT: PSS showed in the diagram in Fig. 10a) and b).

The results obtained in Fig. 11, show a P-n bond between the QD's and the Pedot: PSS, only in the sample at $60°C$ there is no P-n bond due to a large number of defects in the

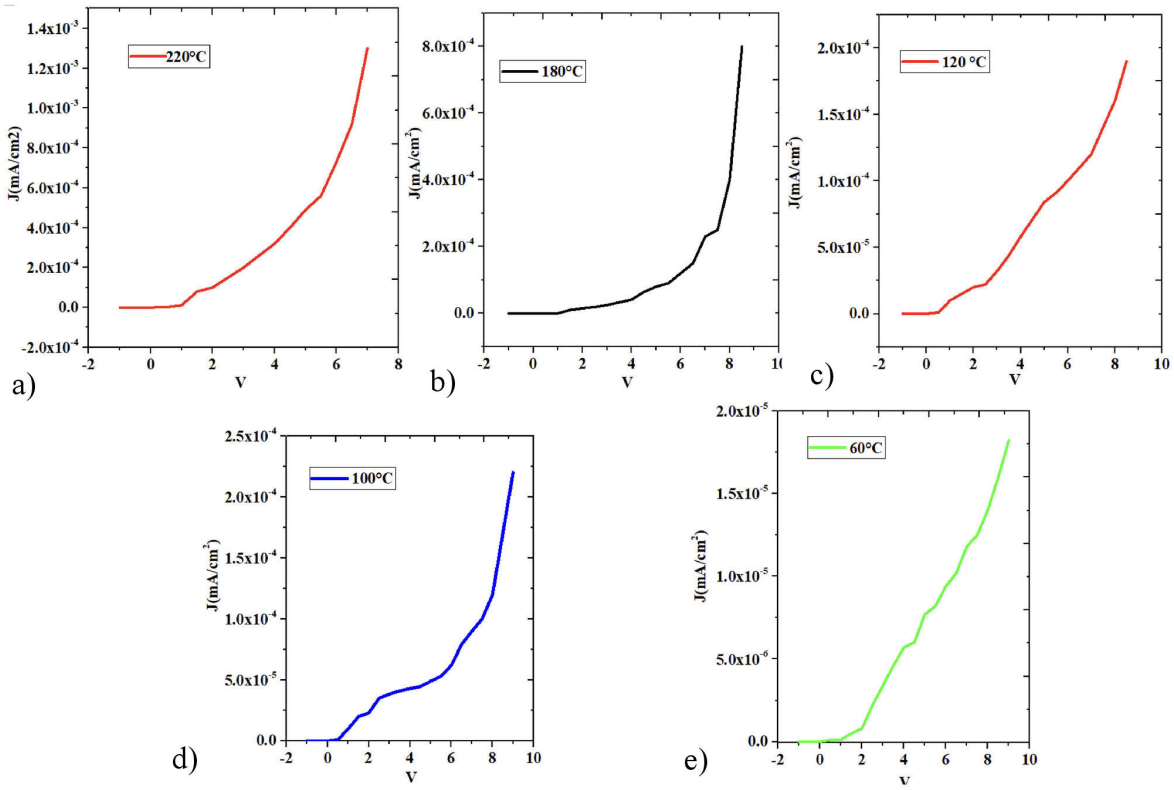

FIGURE 11. Experimental current-voltage (I-V) curve of QDs 220°C, 180°C, 140°C, 100°C and 60°C Schottky diode.

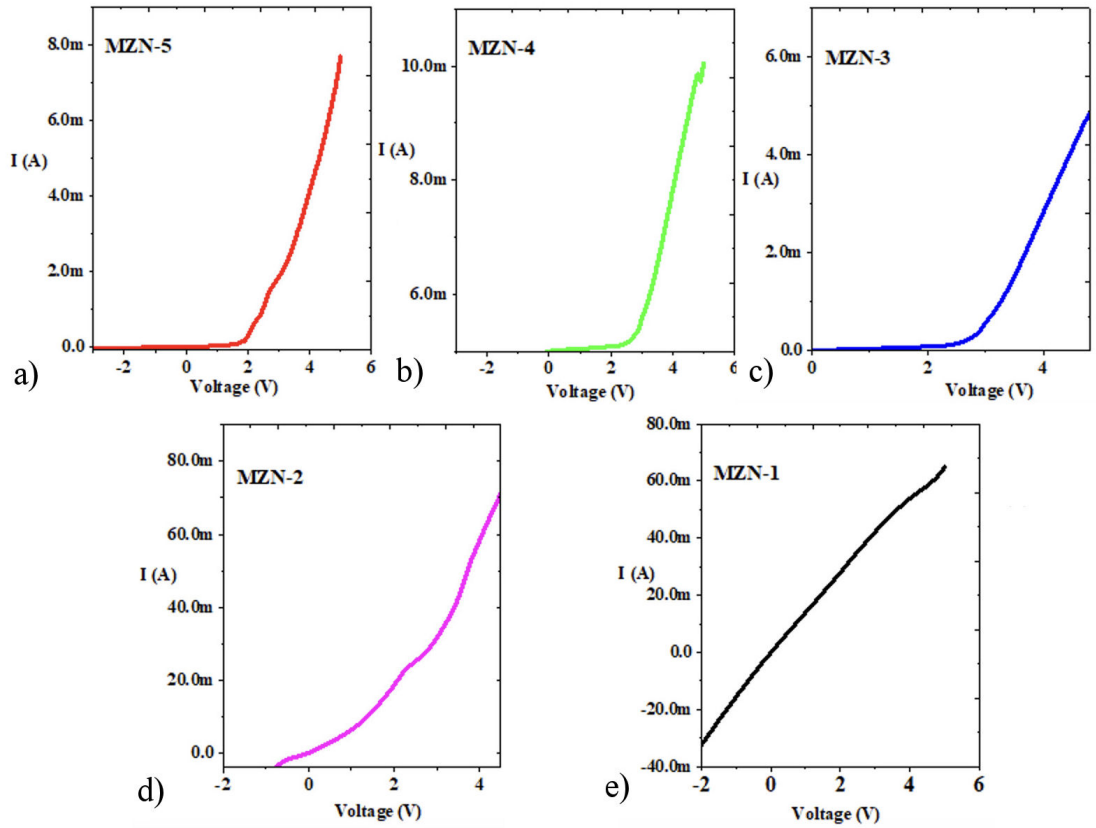

FIGURE 12. Experimental current-voltage (I-V) curve of MZN-1, MZN-2, MZN-3, MZN-4 and MZN-5 Schottky diode.

films, but when the films have the heat treatment of $100 - 220°\mathrm{C}$, P-n bonding is achieved, although the graph does not well-formed, due to the high resistivity and low concentration of carriers. [15].

Figure 12 shows the current-voltage (I-V) MZN-1, MZN-2, MZN-3, MZN-4 and MZN-5. In the ZnO-QDs films, in this analysis, the intrinsic crystalline defects are an important parameter that is associated with the response of the I-V curve. According to Table IV, it is possible to relate the structural behavior of the nanocrystals associated with the electrical phenomena examined here. The experimental results are registered considering the optimum calcination temperature in the crystalline growth and adequate to obtain the optimum concentration of structural defects. The behavior that considerably governs the Schottky diode responds that in all films it is not possible to obtain the p-n junction. However, in the MZN-5 samples, it is observed in particular that the I-V curve presents the optimal behavior, which is associated with the optimal reduction of intrinsic crystalline defects and the optimal obtaining (p-njunction) of the Schottky diode curve.

4. Conclusions

QD's of ZnO films were applied by varying the heat treatment temperature of $60°\mathrm{C}, 100°\mathrm{C}$, $140°\mathrm{C}, 180°\mathrm{C}$, and $210°\mathrm{C}$ on a diode showing P-n junction, although the I-V curves were better when applying the $\mathrm{ZnO} - \mathrm{QDs}$. Five thin films of $\mathrm{ZnO} - \mathrm{QDs}$ were used to perform the morphological, optical, structural, and electrical analysis. In this manuscript, the key parameter was chosen to find the optimum crystal growth temperature for the chemical synthesis of $\mathrm{ZnO} - \mathrm{QDs}$ thin films. The samples are prepared in parallel by the sol gel technique and colloidal synthesis, respectively, in the range of $60°\mathrm{C}, 100°\mathrm{C}, 140°\mathrm{C}, 180°\mathrm{C}$, and $210°\mathrm{C}$, deposited on glass substrates. SEM investigates the morphological structure of the ZnO-QDs nanocrystals. Compact flakes-like with fibers of compact crystalline conglomerates are observed. In the optical studies of absorbance and transmittance, are registered intrinsic electronic transitions and characteristics of $\mathrm{ZnO} - \mathrm{QDs}$. In particular, the charge-associated transport assigned with the cation $\mathrm{Zn}^{2+} \rightarrow \mathrm{Zn}^{3+} + \mathrm{e}^{-}$, is discussed in this paper. The PL spectra located at the UV-Vis region show the existence of crystalline defects or faults, which are identified with vacancies $(\mathrm{V_{zn}})$, zinc interstices $(\mathrm{Zn_i})$ and oxygen $\mathrm{V_O}$ and $\mathrm{O_i}$, respectively. The experimental study of the Hall Effect, mobility and concentration of charge carriers, and resistivity is recorded and briefly discussed. The p-n junction found in the film MZN-5, presents the relative minimum and therefore optimal concentration performed in this study for the successful construction of the Schottky diode.

Acknowledgments

Authors acknowledge to Ricardo Villegas Tovar Director del Centro de Educación Internacional Vicerrectoría de Investigación y Estudios de Posgrado Torre de gestión académica y servicios administrativos Ciudad Universitaria. Piso 6. Of. 10.

1. H. Fang *et al.,* Realization of the Zn^{3+} oxidation state, Nanoscale **13** (2021) 14041, https://dx.doi.org/10.1039/D1NR02816B.
2. A. Wibowo *et al.,* ZnO nanostructured materials for emerging solar cell applications, *RSC adv.* **10** (2020) 42838, https://doi.org/10.1039/D0RA07689A
3. M. C. Beard *et al.,* Introduction to special issue: Colloidal quantum dots, *J. Chem. Phys.* **153** (2020) 240401, https://doi.org/10.1063/5.0039506.
4. M. Abbas *et al.,* (Bio) polymer/ZnO nanocomposites for packaging applications: a review of gas barrier and mechanical properties, Nanomaterials **9** (2019) 1494, https://doi.org/10.3390/nano9101494.
5. K. Foo *et al.,* Sol-gel derived ZnO nanoparticulate films for ultraviolet photodetector (UV) applications, Optik **124** (2013) 5373, https://doi.org/10.1016/j.ijleo.2013.03.120.
6. S. Raha and M. Ahmaruzzaman, ZnO nanostructured materials and their potential applications: progress, challenges and perspectives, *Nanoscale Adv.* **4** (2022) 1868, https://dx.doi.org/10.1039/D1NA00880C.
7. M. Elkady *et al.,* Construction of zinc oxide into different morphological structures to be utilized as antimicrobial agent against multidrug resistant bacteria, *Bioinorg. Chem. Appl.* **2015** (2015) 536854, https//doi.org/10.1155/2015/536854.
8. A. Kołodziejczak-Radzimska and T. Jesionowski, Zinc oxide-from synthesis to application: *Rev. Mater.* **7** (2014) 2833, https://doi.org/10.3390/ma7042833.
9. I. Ben Amor *et al.,* Sol-gel synthesis of ZnO nanoparticles using different chitosan sources: effects on antibacterial activity and photocatalytic degradation of AZO Dye, *Catalysts* **12** (2022) 1611, https://doi.org/10.3390/catal12121611.
10. W. Lin *et al.,* A general approach to study the thermodynamics of ligand adsorption to colloidal surfaces demonstrated by means of catechols binding to zinc oxide quantum dots, *Chem. Mater.* **27** (2015) 358, https://doi.org/10.1021/cm504080d.
11. K. Tian, B. Tudu, and A. Tiwari, Growth and characterization of zinc oxide thin films on flexible substrates at low temperature using pulsed laser deposition, *Vacuum* **146** (2017) 483, https://doi.org/10.1016/j.vacuum.2017.01.018.
12. L. Zhang *et al.,* Origin of visible photoluminescence of ZnO quantum dots: defect-dependent and size-dependent, *J. Phys.*

Chem. C **114** (2010) 9651, https://doi.org/10.1021/jp101324a.

13. R. Raji and K. Gopchandran, ZnO nanostructures with tunable visible luminescence: Effects of kinetics of chemical reduction and annealing, J. Sci.: Adv. Mater. Devices **2** (2017) 51, https://doi.org/10.1016/j.jsamd.2017.02.002.

14. A. E. Danks, S. R. Hall, and Z. Schnepp, The evolution of 'sol- gel'chemistry as a technique for materials synthesis, Mater. Horiz. **3** (2016) 91, https://doi.org/10.1039/C5MH00260E.

15. M. V. Garrido *et al.*, Analysis of blue (BE), green (GE), yellow (YE), and red (RE) emission band in ZnO quantum dots, Optik **271** (2022) 170102, https://doi.org/10.1016/j.ijleo.2022.170102.

16. A. Rivera-Márquez *et al.*, Quantum confinement and crystalline structure of CdSe nanocrystalline films, *Phys. Status Solidi (a)* **188** (2001) 1059, https://doi.org/10.1002/1521-396X(200112)188:3⟨1059::AID-PSSA1059⟩3.0.CO;2-5.

17. S. H. Jaafar *et al.*, Influence of calcination temperature on crystal growth and optical characteristics of Eu^{3+} Doped ZnO/Zn2SiO4 composites fabricated via simple thermal treatment method, *Crystals* **11** (2021) 115, https://doi.org/10.3390/cryst11020115.

18. G. F. Carrasco *et al.*, Morphological and structural analysis of the $Fe(OH)^3$ and CuS transitions to Fe_2O_3 and CuO, *Optik* **243** (2021) 167377, https://doi.org/10.1016/j.ijleo.2021.167377.

19. Y. Yan *et al.*, Surface-preferred crystal plane growth enabled by underpotential deposited monolayer toward dendrite-free zinc anode, *ACS nano* **16** (2022) 9150, https://doi.org/10.1021/acsnano.2c01380.

20. H. Dashtian, H. Wang, and M. Sahimi, Nucleation of salt crystals in clay minerals: molecular dynamics simulation, *J. Phys. Chem. Lett.* **8** (2017) 3166, https://doi.org/10.1021/acs.jpclett.7b01306.

21. S. Mourdikoudis, R. M. Pallares, and N. T. Thanh, Characterization techniques for nanoparticles: comparison and complementarity upon studying nanoparticle properties, *Nanoscale* **10** (2018) 12871, https://doi.org/110.1039/C8NR02278J.

22. L. Serrano de la Rosa *et al.*, Synthesis of holmium oxide (Ho_2O_3) nanocrystal by chemical bath deposition, *Optik* **216** (2020) 164875, https://doi.org/10.1016/j.ijleo.2020.164875.

23. M. V. Garrido *et al.*, Thin films ZnO-QDs Synthesis applying simultaneously the techniques of colloidal synthesis and sol gel and phenomenon at $Zn^{2+} \rightarrow Zn3++$ e-charge transfer, applied to Shottky diode., Op. (2024). https://doi.org/10.21203/rs.3.rs-2983032/v1.

24. A. M. Castillo-Paz *et al.*, Nano to micro size transition of hydroxyapatite in porcine bone during heat treatment with low heating rates, Progress in Natural Science: Materials International **30** (2020) 494, https://doi.org/10.1016/j.pnsc.2020.06.005.

25. R. G. Pérez *et al.*, Synthesis of CdCO3 in situ-doped- Pb2+ grown by chemical bath, Mater. Lett. **160** (2015) 488, https://doi.org/10.1016/j.matlet.2015.08.034.

26. M. C. Portillo *et al.*, Characterization and growth of doped- PbS in situ with Bi^{3+}, Cd^{2+} and Er^{3+} ions by chemical bath, *Mater. Sci. Semicond. Process.* **72** (2017) 22, https://doi.org/10.1016/j.mssp.2017.09.012.

27. A. A. Mansur *et al.*, Carboxymethylcellulose/ZnCdS fluorescent quantum dot nanoconjugates for cancer cell bioimaging, *Int. J. Biol. Macromol.* **96** (2017) 675, https://doi.org/10.1016/j.ijbiomac.2016.12.078.

28. C. Ciarrocchi *et al.*, Interligand Charge-Transfer Processes in Zinc Complexes, Chemistry **4** (2022) 717, https://doi.org/10.3390/chemistry4030051.

29. A. Janotti and C. G. Van de Walle, Fundamentals of zinc oxide as a semiconductor, *Rep. Prog. Phys.* **72** (2009) 126501, https://dx.doi.org/10.1088/0034-4885/72/12/126501.

30. V. Singh, D. Das, and C. Rath, Studies on intrinsic defects related to Zn vacancy in ZnO nanoparticles, *Mater. Res. Bull.* **48** (2013) 682, https://doi.org/10.1016/j.materresbull.2012.11.026.

31. M. Rahamim, H. Cohen, and E. Edri, Chemistry and charge trapping at the interface of silver and ultrathin layers of zinc oxide, *ACS Appl. Mater. Interfaces* **13** (2021) 49423, https://doi.org/10.1021/acsami.1c11566.

32. Y. Ma *et al.*, Charge transfer-induced photoluminescence in ZnO nanoparticles, *Nanoscale* **11** (2019) 8736, https://doi.org/10.1039/C9NR02020A.

33. A. P. Tarasov, A. E. Muslimov, and V. M. Kanevsky, Excitonic mechanisms of stimulated emission in low-threshold ZnO microrod lasers with whispering gallery modes, *Materials* **15** (2022) 8723, https://doi.org/10.3390/ma15248723.

34. T. Mueller and E. Malic, Exciton physics and device application of two-dimensional transition metal dichalcogenide semiconductors, *npj 2D mater. appl.* **2** (2018) 29, https://doi.org/10.1038/s41699-018-0074-2.

35. J. Zhou *et al.*, Choosing sides: unusual ultrafast charge transfer pathways in an asymmetric electron-accepting cyclophane that binds an electron donor, *Chem. Sci.* **10** (2019) 4282

36. H. Lee *et al.*, Effect of donor-acceptor molecular orientation on charge photogeneration in organic solar cells, *NPG Asia Mater.* **10** (2018) 469, https://doi.org/10.1038/s41427-018-0054-1.

37. M. Patra *et al.*, Synthesis of stable dispersion of ZnO quantum dots in aqueous medium showing visible emission from bluish green to yellow, *J. Lumin.* **129** (2009) 320, https://doi.org/10.1016/j.jlumin.2008.10.014.

38. A. S. SÃ¡nchez *et al.*, Optical and morphological changes in the solid state of chiral imines bearing halogen substituents (F, Cl, and Br), *Mater. Lett.* **189** (2017) 313, https://doi.org/10.1016/j.matlet.2016.11.053.

39. M. V. Garrido *et al.*, Low cost chemical bath deposition synthesis of Zinc Oxide/Zinc sulfide composite and Zinc hydrozincite for methylene blue degradation, *Inorg. Chem. Commun.* **164** (2024) 112484, https://doi.org/10.1016/j.inoche.2024.112484.

40. F. Mao *et al.,* Infrared emission bands and thermal effects for 440-nm-emitting GaN-based laser diodes, *AIP Adv.* **10** (2020) 055311, https://doi.org/10.1063/1.5143802.

41. O. P. Moreno *et al.,* Green emission band associated with defects in the crystal growth of a new chiral imine, *Opt. Mater.* **84** (2018) 646, https://doi.org/10.1016/j.optmat.2018.07.060.

42. M. C. Portillo *et al.,* Structural and optical properties of ZnO nanocrystals growth by the chemical bath deposition, *Optik* **157** (2018) 125, https://doi.org/10.1016/j.ijleo.2017.11.062.

43. L. Al-Farsi *et al.,* pH Controlled Nanostructure and Optical Properties of ZnO and Al-doped ZnO nanorod arrays grown by microwave-assisted hydrothermal method, *Nanomaterials* **12** (2022) 3735, https://doi.org/10.3390/nano12213735.